Ocean Engineering 311 (2024) 118798

Contents lists available at ScienceDirect

Ocean Engineering

journal homepage: www.elsevier.com/locate/oceaneng

Research paper

Seismic response of jacket-supported offshore wind turbines for different operational modes considering earthquake directionality

Carlos Romero-Sánchez *, Luis A. Padrón

Instituto Universitario de Sistemas Inteligentes y Aplicaciones Numéricas en Ingeniería (SIANI), Universidad de Las Palmas de Gran Canaria (ULPGC), Las Palmas de Gran Canaria, 35017, Spain

ARTICLE INFO

Keywords:
Offshore wind turbines
Jacket
Operational modes
OpenFAST
Ground motion directionality
Soil–structure interaction

ABSTRACT

This study aims to analyse how jacket-supported OWTs functioning in three different operational modes (power production, emergency shutdown and parked mode) respond to seismic actions when subject to different incoming wind directions and ground motion shaking directions. To do so, the seismic response of the NREL 5 MW OWT founded on the OC4 jacket substructure is simulated using an OpenFAST model that includes multi-support seismic input, soil–structure interaction and kinematic interaction. The impact of the working conditions and of the directionality of the loads on the jacket substructure is analysed and discussed. The tower top accelerations and displacements are examined for different sets of cases, and the seismic response of the jacket is studied in terms of internal forces and von Mises stresses along the different levels of the substructure. The results show, and quantify, the relevance of considering the different operational modes for a correct design of the substructure and of the foundation. The maximum structural stresses within the jacket substructure appear almost always in power production, with the exception of the top part of the legs, where higher stresses arise during emergency shutdown in several cases.

1. Introduction

Offshore wind technology is an increasingly cost-competitive and reliable source of renewable energies in constant expansion (Global Wind Energy Council, 2023). This expansion is boosting the interest for planning new offshore wind farms at greater sea depths, which encourages the use of jackets as support structures for fixed-bottom Offshore Wind Turbines (OWTs). In fact, for future proposed projects, there is a growing trend towards using jackets due to the increase in maximum water depths for fixed-bottom offshore wind energy (Musial et al., 2023). In recent years, projects with fixed-bottom offshore wind turbines at water depths of more than 60 and 70 metres have been announced (Musial et al., 2023).

Seismic-prone regions are also being increasingly considered for new offshore wind farms, which adds earthquake loads as a potentially critical design aspect. Thus, in such locations, structural design shall take into account the influence of damages caused by a combination of seismic and environmental loads. To do so, the standards (IEC, 2020; DNV, 2014) contemplate different operational modes for the wind turbine. More precisely, three typical operational modes are considered in the seismic response analysis (power production, parked mode and emergency shutdown). In the case of power production, the wind turbine continues to be in operation when an earthquake is detected. In the second operating state, the turbine is in a standstill or an idling condition. In the third scenario, emergency shutdown, the system rapidly disconnects the generator upon detecting a seismic load.

Two different approaches are generally considered when evaluating the seismic response of OWTs: nonlinear simulations in time domain or the response spectrum method (IEC, 2020). The combined effect of aerodynamic and seismic loadings considering the different operational modes should be computed in time domain analyses. Recent studies assume this approach for analysing the dynamic response of monopile-supported offshore wind turbines subjected to an earthquake event (Katsanos et al., 2017; Zuo et al., 2018; Asareh et al., 2016; Padrón et al., 2022; Zuo et al., 2019; Yang et al., 2019; Xi et al., 2023). On the basis of the results of the three typical operating scenarios, a fragility analysis was performed in monopiles substructures by Katsanos et al. (2017), highlighting the relevance of the earthquake excitations for the design of offshore wind turbines. Using a 3D FEM Abaqus model, and considering a specific case, Zuo et al. (2018) concluded that the maximum displacements at the top of the tower when the wind turbine rotates are larger than those when the wind turbine is in parked condition, although opposite conclusions were found, for instance, by Alati et al. (2015) and Yang et al. (2019) for similar problems. Padrón et al. (2022) analysed the seismic behaviour of

* Corresponding author.
E-mail addresses: carlos.romero@ulpgc.es (C. Romero-Sánchez), luis.padron@ulpgc.es (L.A. Padrón).

https://doi.org/10.1016/j.oceaneng.2024.118798
Received 26 April 2024; Received in revised form 16 July 2024; Accepted 21 July 2024
Available online 31 July 2024

monopile-supported OWTs of different rated powers and found that the way in which operational mode and dynamic soil–structure interaction influence the seismic response of the OWT depends on the size and rated power of the turbine, among other aspects. Zuo et al. (2019) investigated the dynamic behaviours of OWTs subjected to combined environmental and earthquake excitations in the power production and parked modes, considering offshore and onshore seismic motions. They concluded that, compared to the offshore earthquake ground motions, using onshore seismic motions as inputs in the analysis may underestimate the response of the OWTs in both modes of operation.

Another relevant factor in the study of the seismic response of OWTs under different operational modes is the environmental and ground motion directions. Yang et al. (2019) stated that the relative orientation of the ground motion with respect to the wind direction causes significant differences in the structural behaviour, highlighting the impact of the misalignment between the direction of the ground motion and of the environmental loads. In this regard, the effect of the different misalignments between wind and shaking on the combined seismic and aerodynamic loads for different operational scenarios has not been investigated in detail. Mo et al. (2021) performed a seismic fragility analysis of a monopile-supported OWT under different operational scenarios considering the ground motion directionality. They noted that the aerodynamic damping amplified the effect of shaking directionality in normal operation and suggested that the directionality of the ground motion, the wind and waves loads, and the aerodynamic damping should be taken into account in seismic analysis for OWTs. Additionally, Ishihara et al. (2024) studied the effects of combined seismic and aerodynamic loads for different operational modes. Here, the effect of the misalignment between loads is studied for a gravity foundation supporting the OWT, case for which it is found that the maximum tower base moments are obtained in power production.

The influence of the different operational modes of the turbine on the seismic response of the system in the case of jacket support structures has been explored in significantly less studies than for the monopile configuration. The dynamic behaviour of the jacket considering the wind and wave directions was studied by Cheng et al. (2023), who found that the emergency shutdown and parked modes played a significant role in the computed fragilities of severe damage states of the tower and the jacket substructure. Similarly, Alati et al. (2015) presented a study on the seismic response of jacket substructures under combined wind-wave-earthquake loadings for different load cases and found that structural stress demands are highly influenced by the operational mode. Ju and Huang (2019) studied the NREL 5 MW jacket-type OWT and concluded that the combination of seismic and environmental loads during power production often control the structural design in a jacket substructure. In addition, James and Haldar (2022) analysed the utilization of tubular members of the jackets in terms of yield stress considering multidirectional ground motion. They showed the need of considering higher modes and multidirectional ground motion on the seismic analysis of OWTs. The top and bottom sections of the jacket leg were found to be the most critical elements.

The analysis of the body of research outlined above reveals that there exists a clear influence of the different operational modes and of the misalignment between wind and ground motion direction on the dynamic response of the substructures. It is also clear that the response of jacked support structures is not as well studied as that of its monopile counterpart. For these reasons, this study aims to analyse the effects of the different operational scenarios on the structural response of jacket-supported offshore wind turbines considering wind and seismic ground motion directionality. For monopiles, the substructure is cylindrically symmetrical. However, this is not the case for jackets, so the loads directionality may be more relevant. The seismic response of the OWT under power production was studied in a previous paper (Romero-Sánchez and Padrón, 2024) that showed that load combinations with aligned wind and ground motion directions are never the worst-case scenario in terms of internal forces in the substructure. In this case, the influence of the different operational modes on a four-legged jacket-supported OWT is analysed.

Table 1
Main characteristics of the OWT.

Rating [MW]	5
Rotor diameter [m]	126
RNA mass [ton]	350
Hub height [m]	90.55
Rated wind speed [m/s] (V_r)	11.4
Cut-out wind speed [m/s] (V_{out})	25.0
Tower top height from mean sea level (H_{Top}) [m]	88.15
Tower base height from mean sea level [m]	20.15
Tower top thickness [mm]	30
Tower base thickness [mm]	32
Tower top diameter [m]	4.00
Tower base diameter [m]	5.60
Water depth (W) [m]	50.00
Jacket height (H_{Jacket}) [m]	70.15
Top leg spacing [m]	8.00
Base leg spacing [m]	12.00
Number of bracing levels	4
Number of legs	4
Pile diameter [m]	2.082
Pile thickness [mm]	60.00
Pile depth (L_{Pile}) [m]	34.00

Table 2
Soil profile properties.

Soil profile	Layered
Type of soil	sand
Poisson's ratio, ν_s [–]	0.35
Density, ρ_s [kg/m^3]	2000
Shear modulus, G_s [MPa]	42.6 ($0 < z < 5$ m)
	61.9 ($5 < z < 14$ m)
	87.4 ($14 < z < \infty$)
Shear wave velocity, v_s [m/s]	145.9 ($0 < z < 5$ m)
	175.9 ($5 < z < 14$ m)
	209.0 ($14 < z < \infty$)
Damping, ζ_s [–]	0.05

The paper is organized in five sections. The problem definition is described in Section 2, where the jacket substructure for the NREL 5 MW OWT, the pile foundations, the characteristics of the stratified soil, the seismic signals and the set of cases for the analysis, are specified. Section 3 summarizes the numerical model employed for the parametric analysis, a modified OpenFAST model that includes soil–structure interaction, kinematic interaction and multi-support seismic input motion. The dynamic structural behaviour of the jacket substructure and the comparative analysis of the different operational modes are presented and discussed in Section 4, while the conclusions from the study are presented in Section 5.

2. Problem definition

2.1. Offshore wind turbine properties

The reference NREL 5 MW three-bladed turbine, as described in Jonkman et al. (2009), is assumed to be installed on the four-legged jacket substructure detailed in the OC4 project (Vorpahl et al., 2011). Vertical piles with a diameter of 2.082 m and a length of 34 m are assumed as foundation under each leg. Steel material properties are: Young's modulus 210 GPa, shear modulus 80.8 GPa, mass density 7850 kg/m^3 and damping ratio 2%. Table 1 summarizes the main characteristics of the system. The jacket consists of numerous tubular elements joined together, and organized in 4 bracing levels. Fig. 1 illustrates the levels of the jacket substructure and the different loads considered in the study. The soil profile properties, defined according to the parameters of the three layer sandy soil used in Jonkman and Musial (2010), Løken and Kaynia (2019), are shown in Table 2.

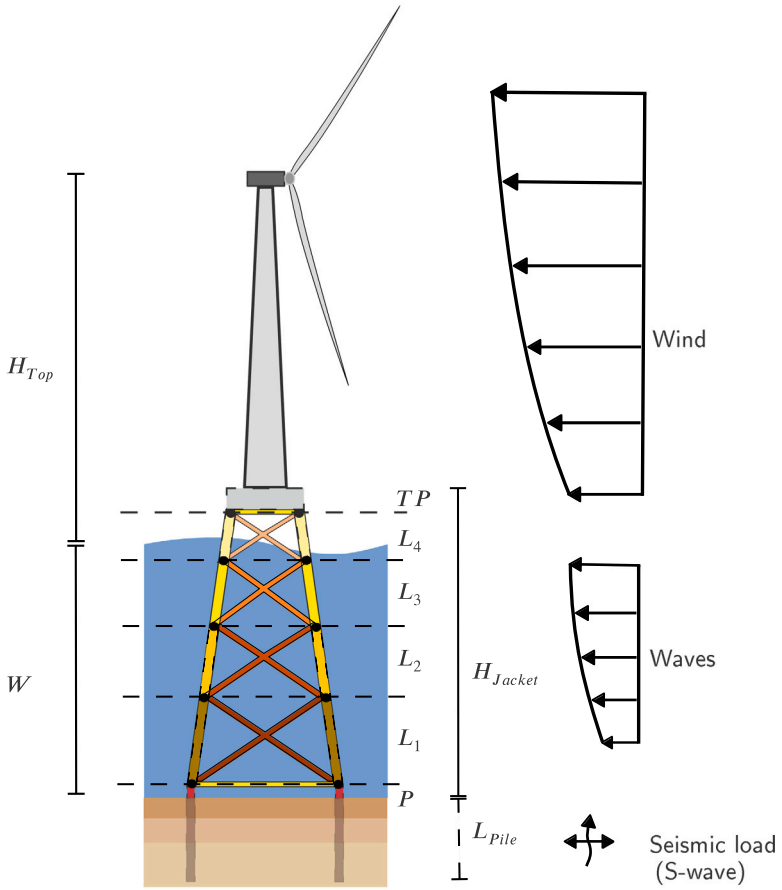

Fig. 1. Representation of the jacket-supported OWT subjected to wind, wave and earthquake loads.

2.2. Operational conditions

In this paper, the dynamic response of the OWT considering dynamic soil–structure interaction is studied for the different operational modes: power production (PP), emergency shutdown (ES) and parked mode (PM). According to IEC61400-1 (IEC, 2020), the earthquake loading shall be superposed with operational loading equal to the higher of: (a) earthquake with power production during normal operation (V_r); (b) loads during emergency stop at rated wind speed (V_r); and (c) loads during idling or parked condition at the cut-out wind speed (V_{out}).

For the power production scenario, when the earthquake arrives, the wind turbine is assumed to continue in operation. Environmental loads are defined according to IEC 61400-3 (IEC, 2021). The turbulent wind fields (Kaimal spectrum) are computed using Turbsim (Jonkman, 2009) for a mean wind speed at hub V_r = 11.4 m/s, assuming Normal Turbulent Model (NTM (IEC, 2020)) and Category B turbulent wind fields. The aerodynamic forces on blades and tower are computed using the Blade Element Mode (BEM) theory in the AeroDyn module (Moriarty and Hansen, 2005). The hub is positioned according to the wind direction. The Hydrodyn module is employed to compute the hydrodynamic loads considering regular and irregular waves (JONSWAP spectrum). The significant height and peak spectra period are defined in Table 4. The wind and waves loads act in alignment based on design guidelines (IEC, 2020; DNV, 2014).

For the power production and the emergency shutdown scenarios, the wind loads are generated based on the same rated wind speed (V_r). In the case of emergency shutdown, the generator is disconnected and the blades are pitched to feather with a pitching rate of 8 deg/s when the first significant peak of the earthquake strikes the OWT. The wave peak-spectral period and significant wave height are 10 s and 8 m, respectively.

In the case of the parked mode, the mean wind velocity at hub is assumed to coincide with the cut-out wind speed (V_{out}), i.e., 25 m/s. The significant height of the incident waves is 10 m. Regular and irregular waves are included. In this mode, blade pitch angle is set to 90°, so the aerodynamic load is insignificant compared with the other loads.

2.3. Ground motion selection

The system is assumed to be excited by vertically propagating shear waves (S-waves). Four different accelerograms are used to obtain the seismic response in the OWT. The acceleration signals are extracted from two different databases, PEER Ground Motion Database (Pacific Earthquake Engineering Research Center (PEER), 2022), and K-NET (National Research Institute for Earth Science and Disaster Resilience (K-NET), 2022). A recording from an offshore station is extracted from this last database. The earthquakes have been selected according to the average shear waves velocity $V_{s,30}$ measured at the recording location so that its value is similar to the range of $V_{s,30}$ of the soil profile considered in this study. Table 3 shows the main information of the selected accelerograms: name and year of the earthquake event, name of the station and maximum ground acceleration ($a_{g,max}$).

For the purpose of comparing the response to different accelerograms, the ground motion signals were linearly scaled to a Peak Ground Acceleration (PGA) of 0.16 g. This value is representative of a moderate seismic hazard, consistent with the hypothesis of linear structural behaviour and with the recommended recurrence period of 475 years (IEC, 2020) for a site within the seismic zone 2 (structure's exposure level L2 and Seismic Risk Category SRC2) defined by the

Table 3
Details of the accelerograms used in the study (before scaling).

No.	Event name	Station name	$a_{g,max}$(g)	Database	Observations
1	Imperial Valley-06, 1979	Niland Fire Station	0.11	PEER	Onshore (RSN:186, Dir: 90°)
2	Superstition Hills-02, 1987	El Centro Imp. Co. Cent.	0.36	PEER	Onshore (RSN:721, Dir: 0°)
3	Loma Prieta, 1984	Hollister City Hall	0.22	PEER	Onshore (RSN:777, Dir: 180°)
4	Miyakejima, 07/30/2000	Hiratsuka-ST1	0.19	K-NET	Offshore (33.97N,139.40E, Dir: N-S)

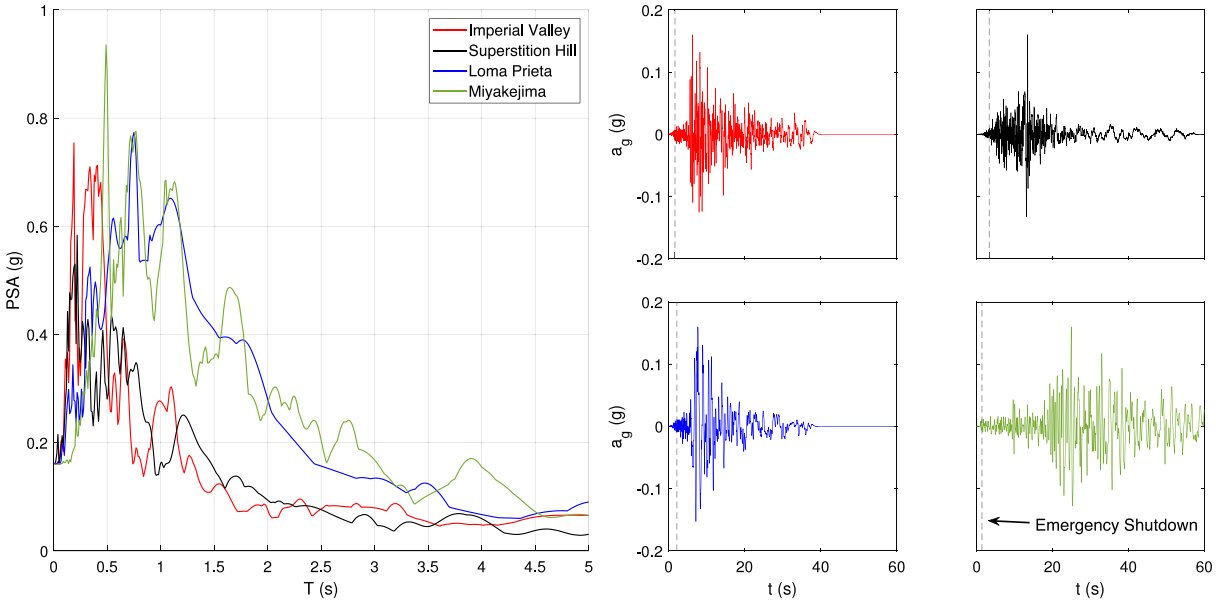

Fig. 2. Normalized pseudo-spectral accelerations (PSA) and ground acceleration (a_g) of the selected seismic signals. The vertical dashed lines mark the time at which ES is triggered in each case.

ISO 19901-2 (ISO 19901-2, 2022). The recurrence period corresponds to a probability of occurrence of 10% in 50 years, which is the one established by Eurcode 8 - Part 5 (2018) for performing seismic verifications. Fig. 2 represents the normalized acceleration spectra and the ground acceleration of the seismic records considered.

2.4. Environmental and earthquake loads combinations

In order to analyse the effects of the operational modes and of the misalignment between environmental and earthquake loads on the seismic response of the jacket substructure, different combinations of these parameters are studied. Different wind directions are established from $\theta_w = 0°$ to $\theta_w = 90°$ ($\Delta\theta_w = 15°$), while the ground motions are rotated from $\theta_s = 0°$ to $\theta_s = 180°$ with intervals of $\Delta\theta_s = 15°$. Fig. 3 shows a graphical overview of the different load combinations used in the analysis, and Table 4 presents a summary of the combinations analysed, resulting in a total of 1113 different simulations. Note that the hub is always oriented in the direction of the wind. The turbine is simulated in the three operational modes (power production, emergency shutdown and parked mode) mentioned above, as described in IEC-61400-1 (IEC, 2020) and DNV-ST-0437 (DNV, 2016) for seismic analysis. The simulation duration is 300 s in each case. In all cases, the ground motion was applied at the start of the 200 s in order to avoid the primary transient behaviour of the system.

3. Methodology

3.1. Numerical model

The seismic response of the system is computed through the code OpenFAST (National Renewable Energy Laboratory, 2024). OpenFAST is a multi-physics tool for simulating the coupled dynamic response of wind turbines. It consists of different computational modules (AeroDyn, HydroDyn, ServoDyn, ElastoDyn and SubDyn) that enable coupled nonlinear aero-hydro-servo-elastic simulation in time domain. The OpenFAST framework employs a modular approach, wherein the models that simulate different aspects of the system are programmed into modules that interact in a loosely coupled time-integration scheme through a glue code that controls and coordinates the simulation, transferring data among modules at each time step. Each module integrates its equations through its own solver. In order to be able to address the seismic analysis of the jacket-supported OWTs, the SubDyn module (Damiani et al., 2015) (that models the dynamic response of the substructure) was modified to include dynamic soil–structure interaction and multi-support ground input motion. This modification allows to consider horizontal, vertical and rotational foundation input motion on multi-support substructures. The elements in the jacket substructure are modelled as Euler–Bernoulli three-dimensional beams. The Craig–Bampton method is used to reduce the number of the internal generalized degrees of freedom of the substructure. The results obtained in OpenFAST are post-processed to obtain the internal forces along the entire length of the elements.

The equation of motion is described in Eq. (1), where the motion vectors have been partitioned to separate the response quantities from the input (Clough and Penzien, 1995). Thus, the motion vectors include the degrees of freedom of the structure, $\mathbf{u}(t)$, and the components of the foundation input motions at each support, $\mathbf{u}_g(t)$. The global mass, damping and stiffness matrices have been partitioned accordingly. The matrices related to the forces arising from the motions of the supports are denoted with the subindex g. $\mathbf{F}(t)$ represents the external forces acting at each degree of freedom of the substructure.

$$\mathbf{M}\,\ddot{\mathbf{u}}(t) + \mathbf{C}\,\dot{\mathbf{u}}(t) + \mathbf{K}\,\mathbf{u}(t) = \mathbf{F}(t) - \mathbf{M_g}\,\ddot{\mathbf{u}}_\mathbf{g}(t) - \mathbf{C_g}\,\dot{\mathbf{u}}_g(t) - \mathbf{K_g}\,\mathbf{u_g}(t) \tag{1}$$

The equations are rearranged into a state–space type formulation for time-domain resolution and for coupling with the rest of modules. During each subsequent time step, SubDyn is coupled to ElastoDyn

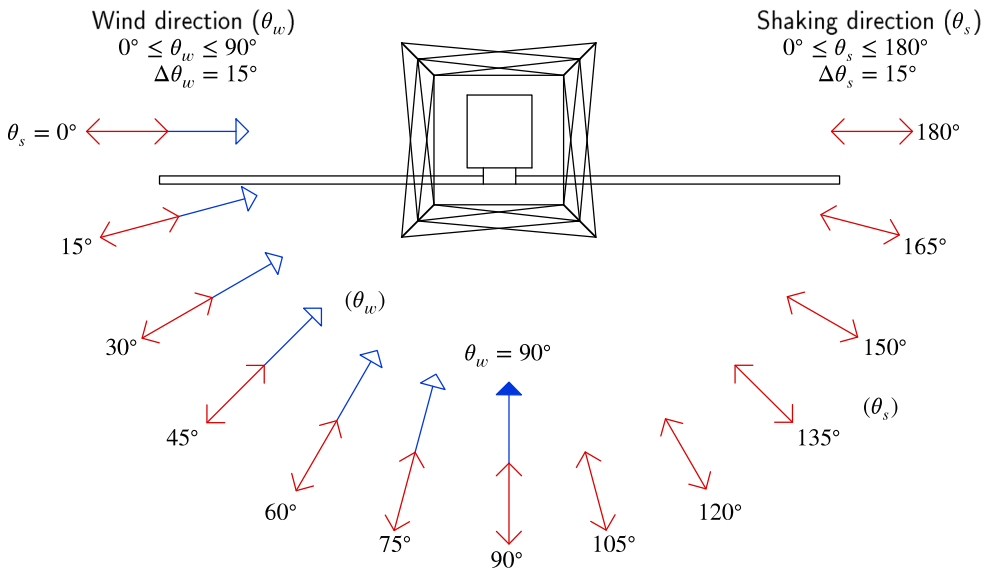

Fig. 3. Definitions of the wind and ground motion directions considered in the study.

Table 4
Summary of the set of cases considered.

Operational mode	Wind loads	Wave loads	Earthquakes	Cases
Power production	Wind speed = 11.4 m/s $0^o \le \theta_w \le 90°$ ($\Delta\theta_w = 15°$)	Significant wave height = 8 m Peak-spectral period = 10 s	4 earthquakes $0^o \le \theta_s \le 180°$ ($\Delta\theta_s = 15°$) or no earthquake	371
Emergency shutdown	Wind speed = 11.4 m/s $0^o \le \theta_w \le 90°$ ($\Delta\theta_w = 15°$)	Significant wave height = 8 m Peak-spectral period = 10 s	4 earthquakes $0^o \le \theta_w \le 90°$ ($\Delta\theta_w = 15°$) or no earthquake	371
Parked mode	Wind speed = 25.0 m/s $0^o \le \theta_w \le 90°$ ($\Delta\theta_w = 15°$)	Significant wave height = 10 m Peak-spectral period = 10 s	4 earthquakes $0^o \le \theta_w \le 90°$ ($\Delta\theta_w = 15°$) or no earthquake	371

(through the interaction forces between tower and substructure) and HydroDyn (through the hydrodynamics forces) modules. More details about the implementation into the Subdyn module and about the verification of the proposed approach are presented in Romero-Sánchez and Padrón (2023), where the modified version was validated by comparison with the results obtained from a finite-element beam model of a four-legged jacket-supported OWT.

3.2. Soil–structure interaction modelling

The foundation response, including its interaction with the surrounding soil, is represented by impedance functions and kinematic interaction factors (KIFs) which are computed through a previously developed continuum model for the dynamic analysis of pile foundations in layered soils (Álamo et al., 2016). Such continuum model is based on the integral expression of the reciprocity theorem and on specific Green's functions to represent the dynamic response of the layered half space used to model the soil. This model avoids the need to discretize any boundary, which reduces significantly the computational requirements and the numerical errors derived from the surface meshing. The model can be applied to study soils whose properties vary continuously with depth by modelling the continuous non-homogeneity through multiple zone-homogeneous horizontal layers. The lateral $I_u(\omega)$ and rotational $I_\theta(\omega)$ KIFs, complex-valued frequency-domain factors, are defined as the ratio between the pile head displacement or rotation and the free-field motion. The earthquake record is filtered using the standard Frequency Domain Method of response (Chopra, 2017) according to the KIFs. The substructuring procedure is schematically described in Fig. 4.

The soil-foundation subsystem is modelled in SubDyn through a Lumped Parameter Model (LPM) developed and validated by Carbonari et al. (2018) that is introduced in the finite elements model of the substructure as an additional element at mudline level (see Fig. 4). The LPM is fitted to the results of the advanced coupled model of boundary elements and finite elements (BEM-FEM model) described above (Álamo et al., 2016, 2021). This model allows to introduce the most relevant aspects of the dynamic response of the foundation into the OpenFAST time-domain simulation. The details about its implementation into SubDyn can be found in Romero-Sánchez and Padrón (2022).

3.3. Post-processing of results in terms of peak and root mean square functions

The structural seismic response for displacements, accelerations, shear forces and bending moments is computed as:

$$\mathrm{X}(t) = \sqrt{\mathrm{X}_x(t)^2 + \mathrm{X}_y(t)^2} \tag{2}$$

where $\mathrm{X}_x(t)$ and $\mathrm{X}_y(t)$ are the time histories of the responses along fore–aft and side-to-side directions, respectively.

The average peak and root mean square internal forces and stresses at a particular point are computed as:

$$\bar{\mathrm{X}}_{\mathrm{peak}} = \frac{1}{N_s}\sum_{i=1}^{N_s}\left(\max\left(|X_i(t)|\right)\right); \quad \bar{\mathrm{X}}_{\mathrm{rms}} = \frac{1}{N_s}\sum_{i=1}^{N_s}\left(\sqrt{\frac{1}{\mathrm{D}}\sum_{j=1}^{\mathrm{D}}\left(X_{j,i}^2(t)\right)}\right) \tag{3}$$

where $i = 1, 2, ., \mathrm{N_s}$; $\mathrm{N_s} = 4$ is the total number of accelerograms considered; $j = 1, 2, ., \mathrm{D}$; D represents the total number of values during the common significant duration ($\mathrm{D_{a5-95}}$); and $\bar{\mathrm{X}}_{\mathrm{peak}}$ and $\bar{\mathrm{X}}_{\mathrm{rms}}$ represent the average of the peak and root mean square values, respectively.

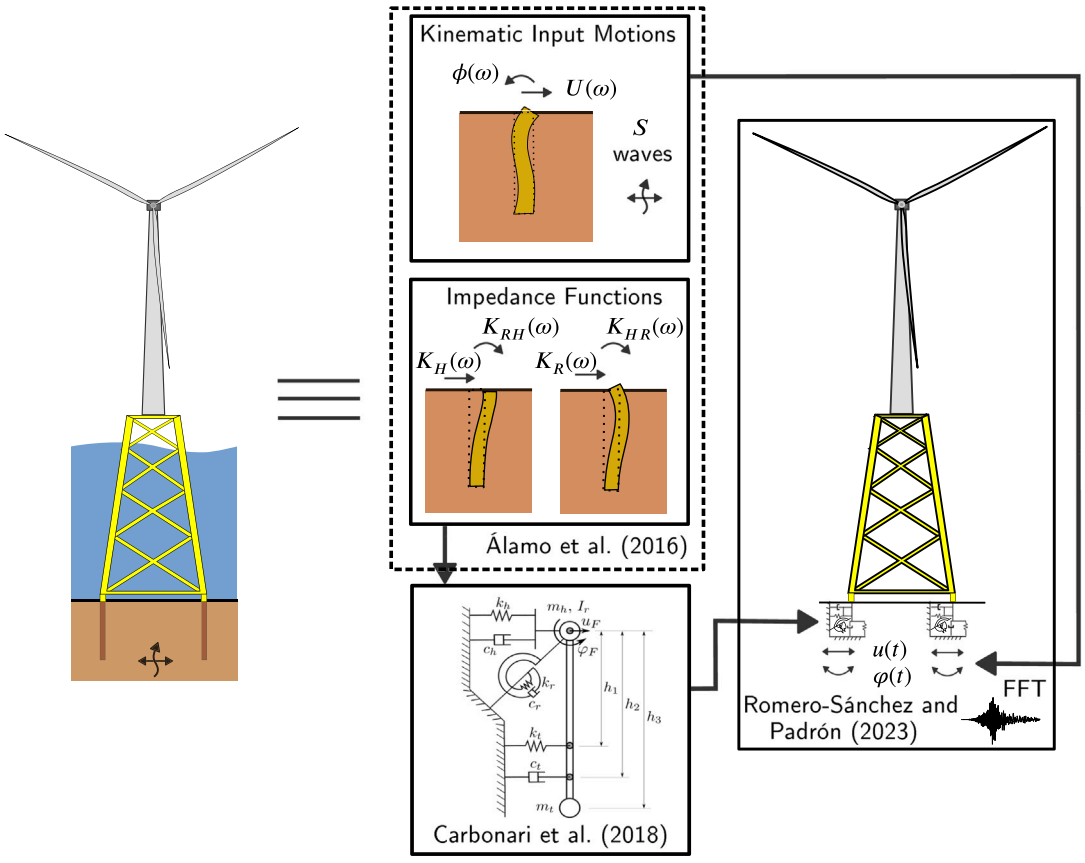

Fig. 4. Schematic soil–structure interaction modelling.

Analysing the results in terms of both peak and root mean square values is crucial to understand whether the trends obtained are consistent across all time responses, rather than just representative of isolated peaks. In this study, root mean square values were computed along the significant duration of each seismic signal. The common D_{a5-95} significant duration (Dobry et al., 1978) is considered, which is defined as the time interval between 5%–95% of the Arias intensity (Arias and Hansen, 1970).

4. Results and discussion

4.1. Displacements, accelerations and internal forces at the tower experienced for the different operational modes

In this section, displacements and accelerations at the tower are analysed for the different operational modes. The displacements are useful for investigating the dynamic behaviour and the magnitude of the response. The tower top accelerations affect the rotor nacelle assembly (RNA), leading to serviceability limitations and influencing the operational lifetime of the wind turbine. In addition, the internal forces obtained at the tower base are analysed.

Fig. 5 presents the tower top displacements of the wind turbine computed for the three different operational modes considered in this study and for a specific illustrative case in which the wind direction considered is $\theta_w = 0°$ and the earthquake (Imperial Valley in this case, chosen for illustration purposes) acts in two different directions, the fore–aft (FA), $\theta_s = 0°$, and side-to-side (SS), $\theta_s = 90°$. The displacements along the fore–aft and side-to-side directions are shown. In the second 200 (earthquake starting), there is a significant increase in the response when the seismic load is applied, highlighting its importance in absolute terms compared to the environmental loads. As expected, the effect of the emergency stop protocol is evident from the history of the tower top displacements along the FA direction. On the other hand, the much smaller relevance of the aeroelastic damping along the SS direction can be clearly seen in Fig. 5(b), as the responses for the three operational modes are very similar to each other and show much less damping that along the FA direction.

Fig. 6 shows the tower top accelerations computed for the same cases considered for Fig. 5. The peak values obtained for each operational mode are highlighted with circles. When the seismic load is considered, the peak acceleration in power production is 5 times higher than that of the reference case without seismic loads. The emergency shutdown scenario presents the highest acceleration in both directions. In contrast, the smallest maximum acceleration is obtained, as expected, for the power production mode when the earthquake acts along the FA direction. This is due to the higher aerodynamic damping, which has a beneficial effect by reducing the magnitude of the vibrations induced by the earthquake (Alati et al., 2015; Meng et al., 2020).

Fig. 7 shows the envelopes of the maximum accelerations along the tower for the FA and SS directions, considering the same cases described above. The maximum accelerations are observed at approximately 70% of the tower height. The accelerations envelopes obtained for the different operational modes differ by up to 90% along the FA direction due to the influence of the aerodynamic damping. Conversely, similar envelopes are observed for the SS direction. Emergency shutdown is the mode that produces the maximum accelerations along the tower in both directions.

The influence of the different load scenarios described in Section 2 can be seen in terms of accelerations in Fig. 8, where the average peak ($\tilde{a}^{TT}_{peak}$) and root mean square ($\tilde{a}^{TT}_{rms}$) accelerations at tower top are shown for the thirteen different ground motion directions and seven wind directions considered in the study. Instead of presenting the results for each individual earthquake, the average values obtained for all seismic

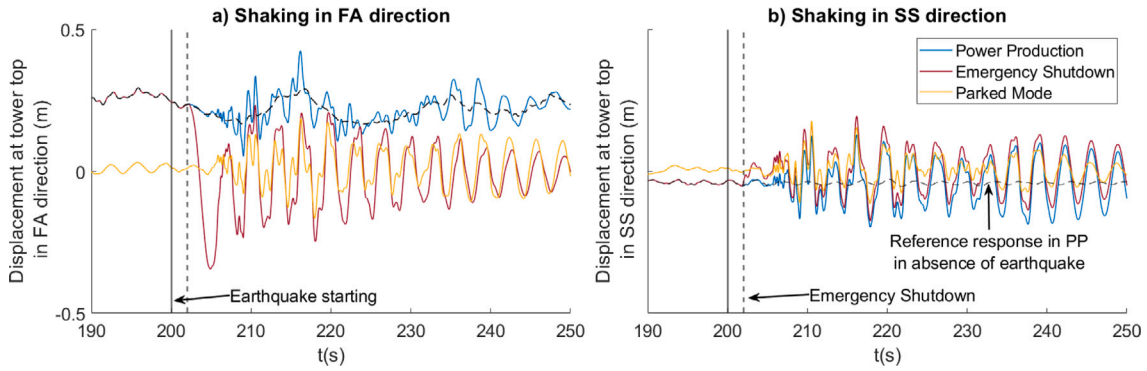

Fig. 5. Time histories of the tower top displacement along FA (a) and SS (b) directions for different operational modes for $\theta_w = 0°$. Imperial Valley. $\theta_s = 0°$ and $\theta_s = 90°$.

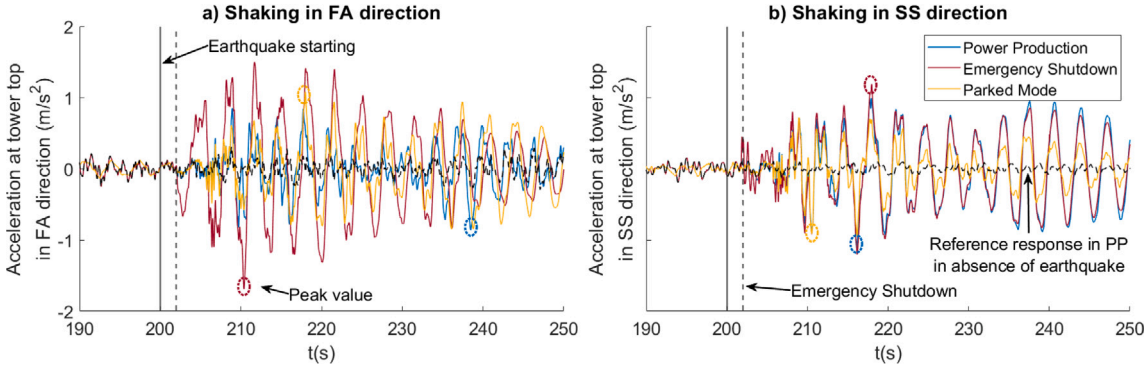

Fig. 6. Time histories of the tower top acceleration along FA (a) and SS (b) directions for different operational modes for $\theta_w = 0°$. Imperial Valley. $\theta_s = 0°$ and $\theta_s = 90°$.

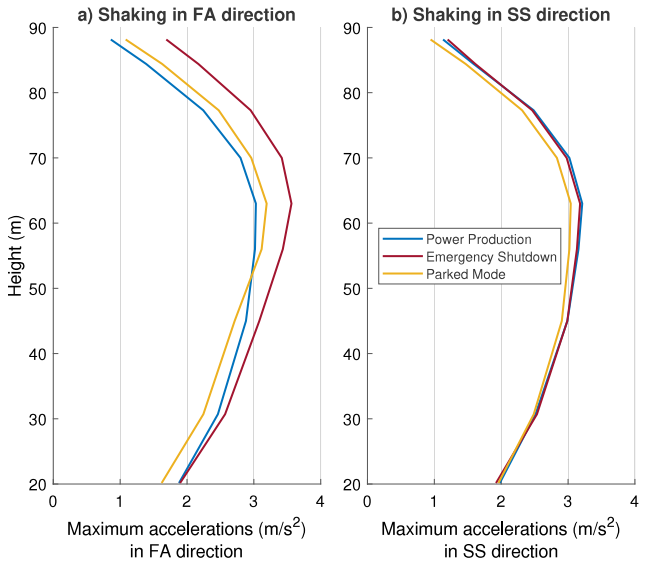

Fig. 7. Acceleration envelopes along the tower for the FA (a) and SS (b) directions for the different operational modes. $\theta_w = 0°$. Imperial Valley. $\theta_s = 0°$ and $\theta_s = 90°$.

loads are presented, as defined in Section 3.3. The results are depicted in polar plot. The accelerations corresponding to the different wind directions (from 0 to 90°) are represented by different colour lines. Two different operational modes, power production (in solid lines) and emergency shutdown (in dashed lines) are shown.

As already observed in Fig. 6, the maximum accelerations at the tower top are obtained for the emergency shutdown scenario. The average peak accelerations obtained for the parked mode (not shown) are lower than those obtained for the power production. At the same time, the highest maximum root mean square accelerations observed during power production are found when shaking occurs along the side-to-side direction. This can be clearly seen when the acceleration is presented in terms of root mean square values. For instance, when $\theta_w = 0°$, the maximum response when the turbine is functioning in power production is found at $\theta_s = 90°$, while for $\theta_w = 90°$, the maximum responses are found for $\theta_s = 0°$ and 180°. At the same time, the curves of these two cases ($\theta_w = 0°$ and $\theta_w = 90°$) cross each other at around $\theta_s = 45°$ and 135° when the turbine is working in such mode. Additionally, for any particular θ_s, the magnitude of the resulting response is clearly ordered from maximum to minimum response when the angle between ground shaking and incoming wind directions change from 0° to ±90°. These trends are due to the variations in the aeroelastic damping (Mo et al., 2021; Romero-Sánchez and Padrón, 2024). However, such tendencies, that are very clear in power production, are not so identifiable under emergency shutdown or parked modes, for which the relevance of the aeroelastic damping is much lower than in power production.

The time histories of the tower base shear force and bending moment for the different operational modes for the case when wind and shaking (Imperial Valley) act along FA direction are shown in Fig. 9. The wind loads exert a significant effect on the structural response in terms of internal forces at the tower base. The maximum internal forces in this particular case are obtained during power production.

4.2. *Effect of wind and ground motion relative directions on the substructure under different operational modes*

The influence of the three different operational modes and of the ground motion directionality on the seismic response of the four-legged jacket-supported OWT is analysed in this section. The response during power production (PP) is studied in Section 4.2.1, during emergency shutdown (ES) in Section 4.2.2 and in parked mode (PM) in Section 4.2.3. In addition, a comparison of the effect of the wind and

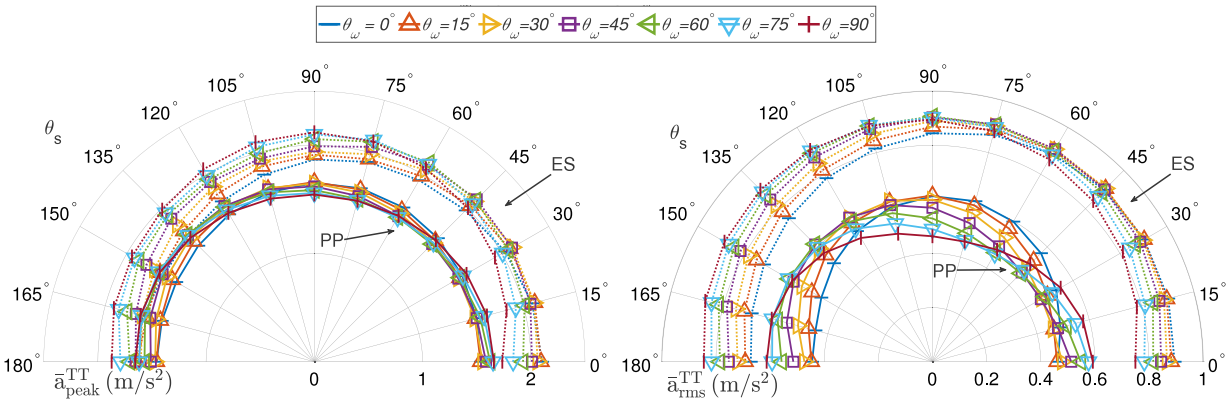

Fig. 8. Average peak and root mean square (rms) tower top (TT) accelerations for the different wind and shaking directions considered in this study in power production and emergency shutdown.

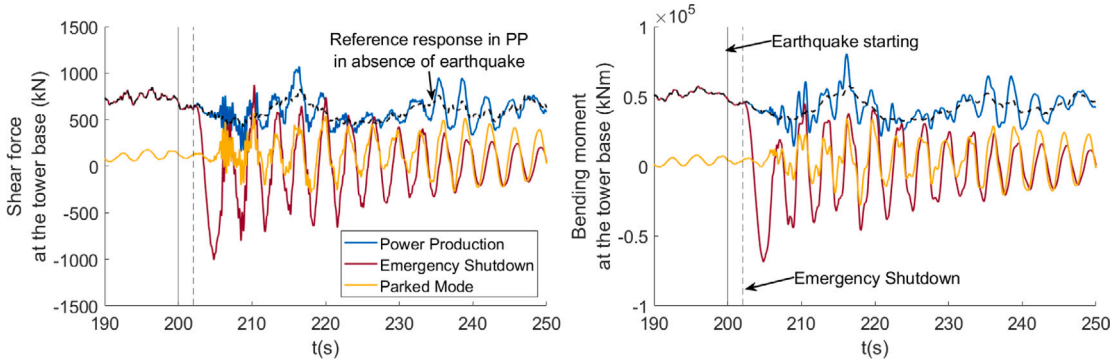

Fig. 9. Time histories of the tower base shear force and bending moment for different operational modes for $\theta_w = 0°$. Imperial Valley. $\theta_s = 0°$.

ground motion relative directions on von Mises stresses and internal forces at the substructure in each operational mode is shown in Section 4.2.4.

4.2.1. Power production

In this section, the peak internal forces and von Mises stresses at the members of the substructure are computed under power production mode. In addition, the effect of the misalignment between wind and ground shaking is analysed for each leg and bracing level of the jacket. To do so, Fig. 10 presents the average peak shear and axial forces obtained at any point of the jacket structure for each combination of wind and ground shaking direction. The points represented in Fig. 10 are located at the connection between leg and transition piece ($\bar{V}^{L4}_{peak}$), and at the joint between leg and pile ($\bar{N}^{L1}_{peak}$), respectively.

The highest average peak shear and axial forces are obtained when the ground shaking acts along one of the diagonals of the jacket (see for instance James and Haldar, 2022), and always arise along sections L4 and L1 (see Fig. 1) of the legs, respectively. The maximum values obtained for both forces are much more dependent on ground shaking direction than on incoming wind direction. In fact, the maximum average peak shear and axil forces vary up to 16% and 25%, respectively, as a function of θ_s, but only up to 4% and 13% as a function of θ_w. Maximum average axial forces are obtained when the earthquake acts within the ranges $30° \leq \theta_s \leq 60°$ and $120° \leq \theta_s \leq 150°$. The results are similar to those obtained for the shear forces, although the influence of wind direction is more relevant than in shear forces.

After having studied the impact of wind and seismic shaking directions (in absolute terms) on the evolution of average peak internal forces in the jacket substructure, it is relevant to analyse their influence in terms of misalignment between ground motion and wind directions ($\Delta = \theta_s - \theta_w$). To do so, Fig. 11 presents the average peak shear and axial forces in bar plot format as a function of the misalignment between loads.

Computed maximum shear forces (see Fig. 11a) are essentially identical for all misalignment angles although, for a given Δ, the values vary for each particular θ_w and the absolute maximum in each case is always obtained when the earthquake acts diagonally. This phenomenon can be clearly observed, for instance, when $\Delta = 0°$ and $\theta_w = 45°$, when $\Delta = 45°$ and $\theta_w = 0°$ ($\theta_s = 45°$) or when $\theta_w = 90°$ ($\theta_s = 135°$). On the other hand, the absolute maximum of the computed average axial peak forces (see Fig. 11b) decreases as the angle of misalignment increases. At the same time, the dispersion decreases and the average value for the different θ_w decreases slightly. Thus, the maximum and minimum mean peak axial force values are both obtained for $\Delta = 0°$. In summary, the internal forces in the four-legged jacket are more influenced by the shaking direction than by the misalignment between wind and shaking direction, although the results show that aligned shaking and wind directions ($\Delta = 0°$) can produce slightly higher maximum axial forces in the substructure.

The behaviour of the jacket for different misalignment angles can also be analysed in terms of amplification ratios defined as:

$$R_{X_{rms}}(\Delta) = \frac{\sum_{i=1}^{n}\left[X_{rms}\left(\theta_{w_i}, \Delta + \theta_{w_i}\right)\right]/n}{\min_{\Delta}\left[\sum_{i=1}^{n}\left[X_{rms}\left(\theta_{w_i}, \Delta + \theta_{w_i}\right)\right]/n\right]} \tag{4}$$

where X_{rms} represents root mean square values of the different internal forces (axial forces $N_{rms}(\theta_w, \theta_s)$, shear forces $V_{rms}(\theta_w, \theta_s)$ or bending moments $M_{rms}(\theta_w, \theta_s)$) for the different combinations of ground motion and wind directions within the range $-90° \leq \Delta \leq 90°$. Each ratio for any given Δ is computed with a combination of seven cases (n = 7).

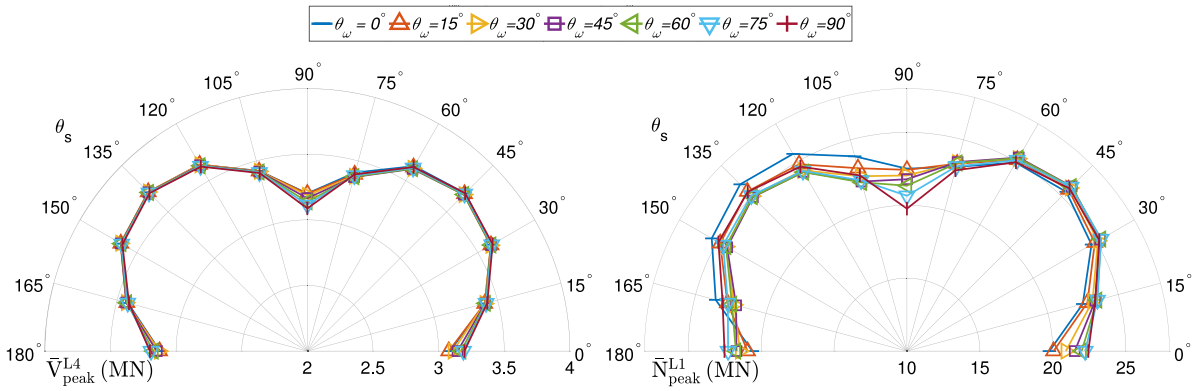

Fig. 10. Average peak response values in terms of shear and axial forces at leg levels 4 and 1, respectively, for the different wind and shaking directions during power production.

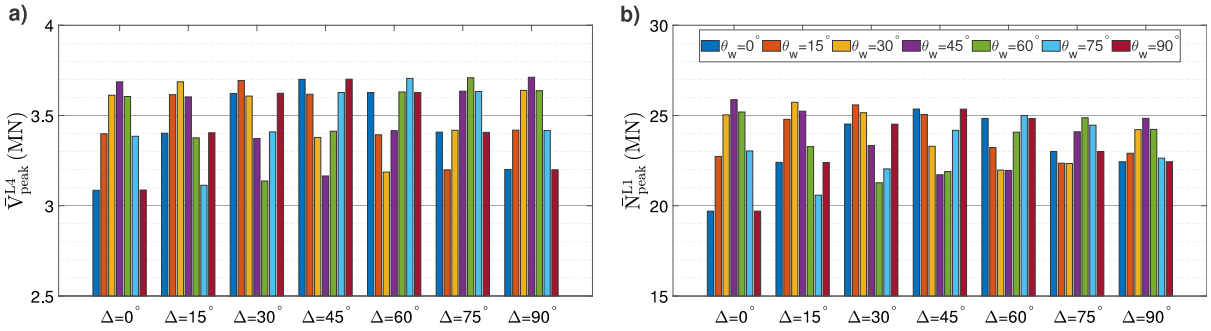

Fig. 11. Average peak response in terms of shear and axial forces at leg levels 4 and 1, respectively, as a function of the misalignment (Δ) between wind and shaking directions during power production.

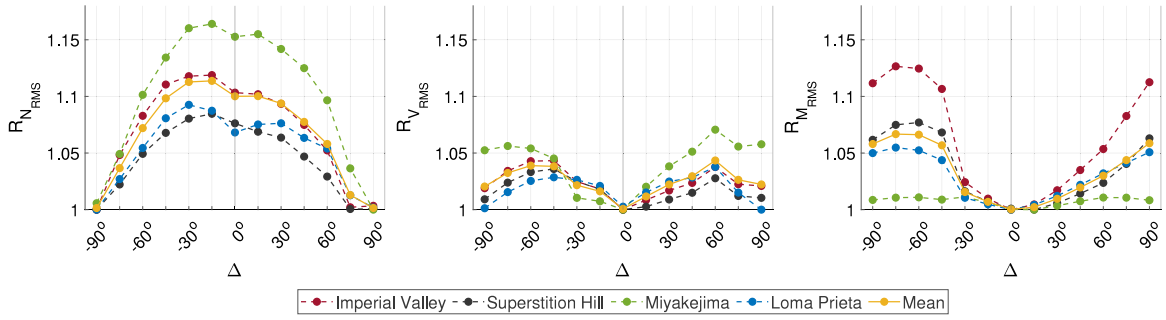

Fig. 12. Amplification ratios for axial forces, shear forces and bending moments at leg levels 1, 4 and pile head, respectively, for the different misalignment angles between wind and ground motion directions during power production.

This amplification factors provide information on how the root mean square values found for a given combination of seismic shaking and wind directions with a certain misalignment between them relate to the case in which such misalignment angle yields the smallest forces. Note that these values are computed for the common significant duration.

Fig. 12 shows the amplification ratios for the three internal forces considered, computed at the points where the peak values are observed, and for each of the earthquakes considered in the analysis. These amplification ratios correspond to the connection between legs and pile in the case of axial forces and bending moments, and to the connection between legs and transition piece in the case of shear forces. The mean response value (orange line) is also shown.

The highest amplification ratios are found for $-15° \leq \Delta \leq -30°$ in the case of axial forces, and for $45° \leq |\Delta| \leq 75°$ in the case of shear forces. The variability of the ratios between different earthquakes in axial forces is higher than in shear forces. The amplification ratio in axial forces reaches a maximum of 16%. For the bending moments, the highest amplification ratios are obtained within the $-75° \leq \Delta \leq -60°$ range. It is important to note the variability between the peak ratios between each of the earthquakes used in the study, despite the use of a common PGA. The maximum mean amplification ratio (11%) is obtained in axial forces.

After analysing the seismic response in terms of internal forces, the behaviour of the jacket is analysed in terms of von Mises stresses, computed as $\sigma_{VM} = (\sigma^2 + \tau^2)^{1/2}$, where σ is the meridional stress and τ is the planar shear stress (Eurocode 3 - Part 1-6, 2007). Fig. 13 presents, for each of the levels of the jacket, the average peak von Mises stresses for all wind and seismic directions. The results corresponding to each one of the levels is shown in a different subplot that presents the average of the maximum values obtained at the point along the element of that level where the maximum stresses appear. The von Mises stresses at the legs and at the bracings elements are represented

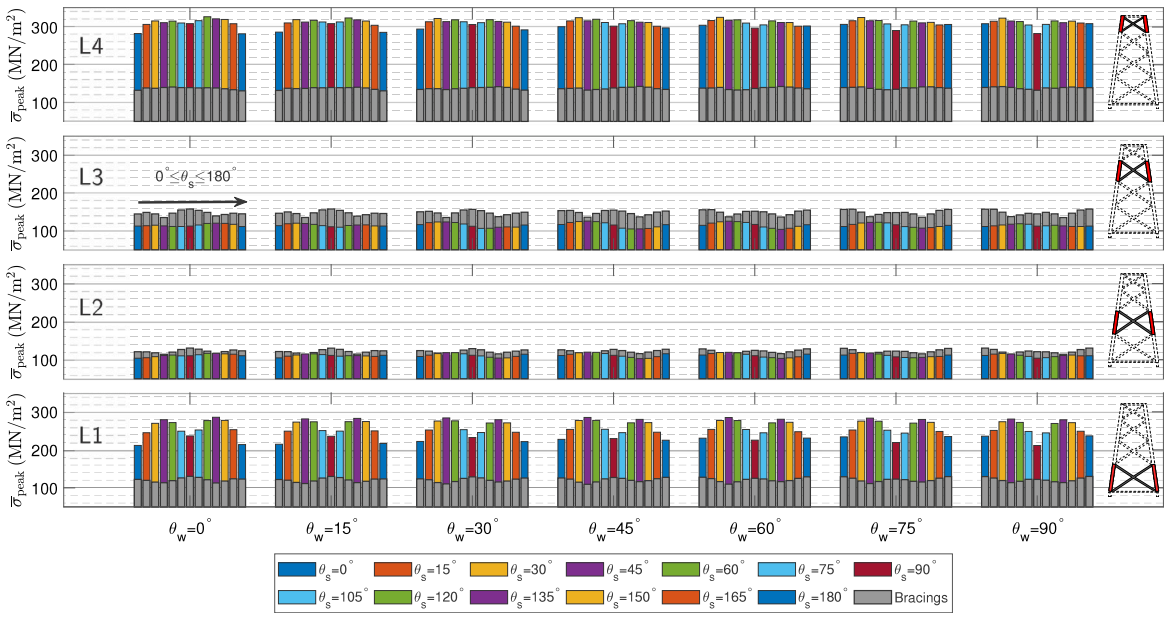

Fig. 13. Average peak response in terms of von Mises stress in the substructure for the different wind and shaking directions during power production. Colour bars are used for stresses in leg members, and grey bars for stresses in the bracing elements (θ_s according to the position).

separately by colour and grey bars, respectively. The sets of bars are ordered for increasing wind directions (θ_w) and, within each set, the bars are ordered for increasing shaking directions (θ_s) from 0° to 180°.

The maximum average stresses arise at level 4 of the leg, at the point where the highest shear forces are obtained, the connection of the leg to the transition piece. In all cases, the jacket zones with the highest stresses are located at the levels 1 and 4 of the main leg, as also found in James and Haldar (2022). Depending on the loads direction, the maximum stresses are found at different legs, but in the same section of the element. Maximum stresses appear when the earthquake direction acts diagonally to the jacket position ($30° \leq |\theta_s| \leq 60°$ and $120° \leq |\theta_s| \leq 150°$), for all wind directions. These ranges coincide with those in which the maximum internal forces are obtained, as shown in Fig. 10. The importance of the aeroelastic damping in the state of power production is observed, for instance, in $\theta_w = 0°$. Similar peak stresses are obtained when the earthquake acts at $\theta_s = 0°$ and $\theta_s = 180°$, but the stress increases when it acts in the side-to-side direction ($\theta_w = 0°$ and $\theta_s = 90°$). Note that the von Mises stresses at levels 2 and 3 are higher in the bracing elements (grey bars) than in the legs. The bracing elements presents similar stresses at all the different levels, in contrast to the legs.

4.2.2. Emergency shutdown

Fig. 14 shows the average peak shear and axial forces obtained at any point of the jacket substructure for all different wind and shaking directions considered in this study. Each colour line represents a different wind direction and the axis of the polar figure represents the shaking direction.

Similarly to what was observed for power production mode, the maximum average shear forces occur when the shaking direction acts along the diagonal of the jacket substructure, specifically within the ranges $30° \leq \theta_s \leq 60°$ and $120° \leq \theta_s \leq 150°$. The maximum axial forces are found for $120° \leq \theta_s \leq 150°$. It can be noted that the lowest forces arise when the shaking direction is midway between two legs, $\theta_s = 0°, 90°$ or 180° (see Fig. 3). Wind load directionality (θ_w) presents a greater influence on the axial forces than on the shear forces, in fact, the shear forces are almost independent of the wind direction, depending almost exclusively of the shaking direction (θ_s).

Fig. 15 represents the amplification ratios for the three internal forces considering emergency shutdown, computed at the points where the peak values of each of the internal forces is observed, and for each of the earthquakes considered in the analysis. Similar trends to those observed in the power production case are obtained, but with lower axial and shear forces amplification ratios. The importance of the misalignment is much lower than that observed in power production mode. This is due to the smaller wind loads arising after the emergency stop, as they decrease as the blades pitch to feather. In the cases of axial and shear forces, the range of the worst-case scenario is $30° \leq |\Delta| \leq 60°$ and the maximum value is around 5%. In the bending moments, the highest ratios are obtained for $-75° \leq \Delta \leq -60°$ and the mean amplification is higher (8%) than during power production. The maximum amplification ratios vary significantly between different earthquakes for bending moments (10%), but not for shear forces.

Fig. 16 presents the average peak von Mises stresses corresponding to the emergency stop situation for all wind and seismic directions. Considering that the emergency shutdown is beneficial in terms of stresses is not clear (see Fig. 13). Despite the lower aerodynamic load on the system, the legs present similar stresses to those obtained in power production mode. The highest values are obtained when the shaking acts along the diagonal direction of the jacket, $30° \leq \theta_s \leq 60°$ and $120° \leq \theta_s \leq 150°$. These ranges coincide with those obtained during power production. Von Mises stresses are similar or higher than during power production at the level 4 of the main leg, the level with the highest peak stress. In the emergency shutdown mode, the bracing level with the highest von Mises stresses is the level 3.

4.2.3. Parked mode

Fig. 17 presents the average peak shear and axial forces obtained at any point at the jacket substructure, considering the seven different wind directions and thirteen shaking directions. The angle of the wind direction is represented by different colour lines and the shaking direction is shown in the axis of the polar plot.

The maximum shear and axial forces are found at the legs, specifically at the level 4 and 1, respectively. The influence of the aerodynamic damping is not relevant in parked mode, The variation of the wind direction has practically no influence. The results obtained are very similar in fore–aft ($\theta_s = 0$) or side-to-side ($\theta_s = 90$) directions. The parked mode presents peak internal forces lower than those obtained during power production and emergency shutdown. The highest axial

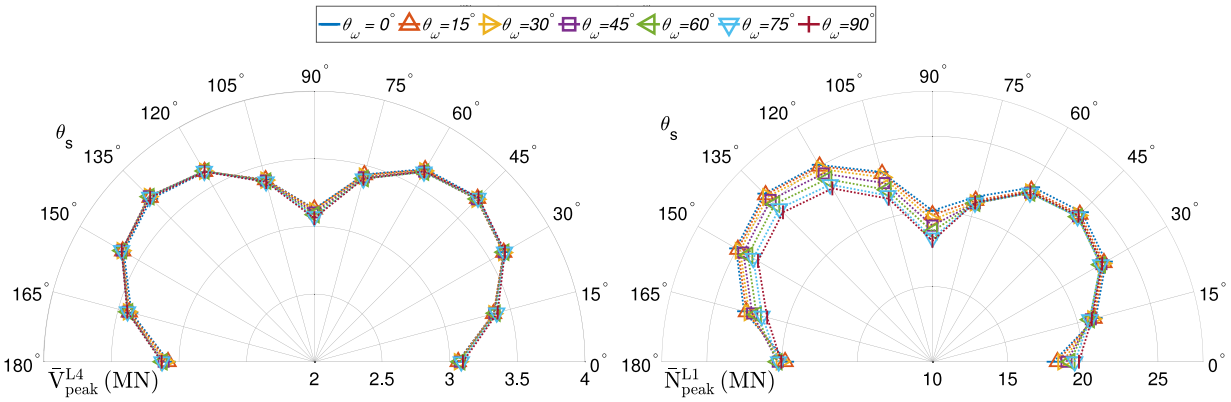

Fig. 14. Average peak response values in terms of bending moments and axial forces at leg levels 4 and 1, respectively, for the different wind and shaking directions considering emergency shutdown.

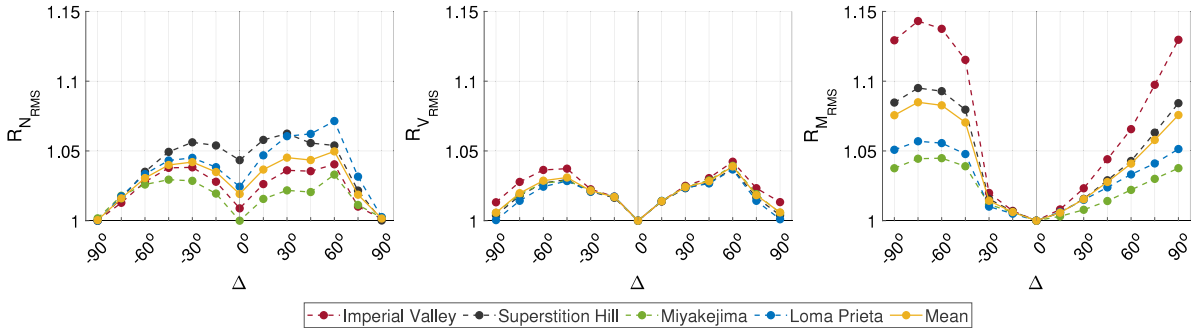

Fig. 15. Amplification ratios for axial forces, shear forces and bending moments at leg levels 1, 4 and pile head, respectively, for the different misalignment angles between wind and ground motion directions considering emergency shutdown.

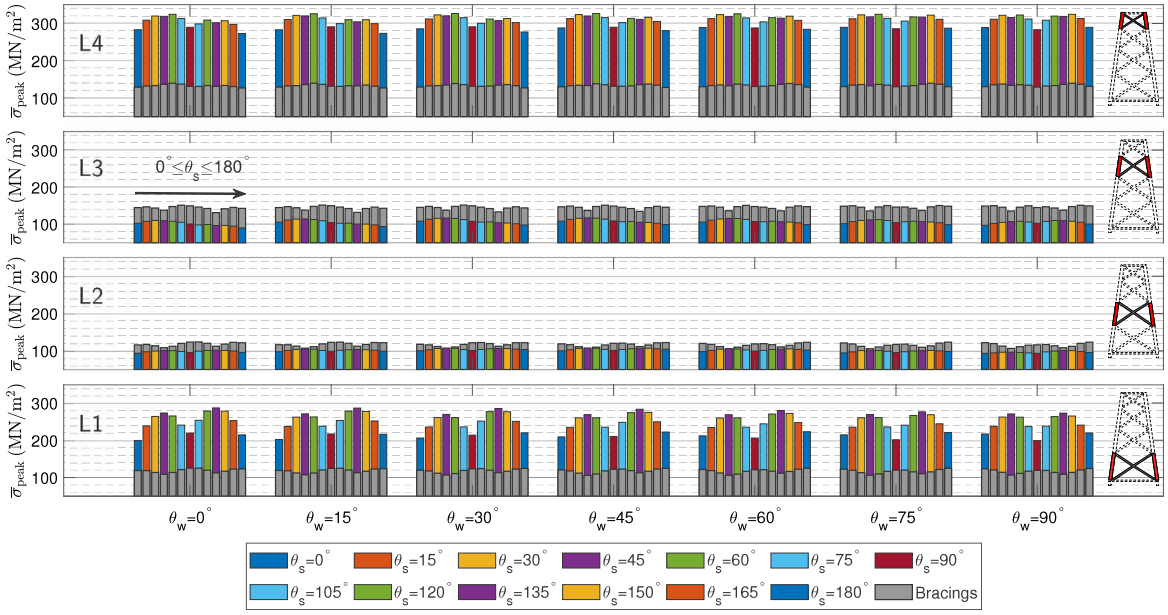

Fig. 16. Average peak response in terms of von Mises stress in the substructure for the different wind and shaking directions considering emergency shutdown. Colour bars are used for stresses in leg members, and grey bars for stresses in the bracing elements (θ_s according to the position).

and shear forces are obtained when earthquake loads act along the diagonal direction. In short, significant differences in the peak forces are only observed with the change of the shaking direction.

Fig. 18 presents the amplification ratios for the three internal forces considered, computed at the points where the peak values are observed in the jacket substructure, and for the four seismic loads considered. The orange line represents the mean response value of the different accelerograms.

In this working condition, the amplification ratios are lower than during power production in terms of axial and shear forces, but the values are similar to those obtained in emergency shutdown mode. The lowest ratios are obtained when the misalignment between wind and

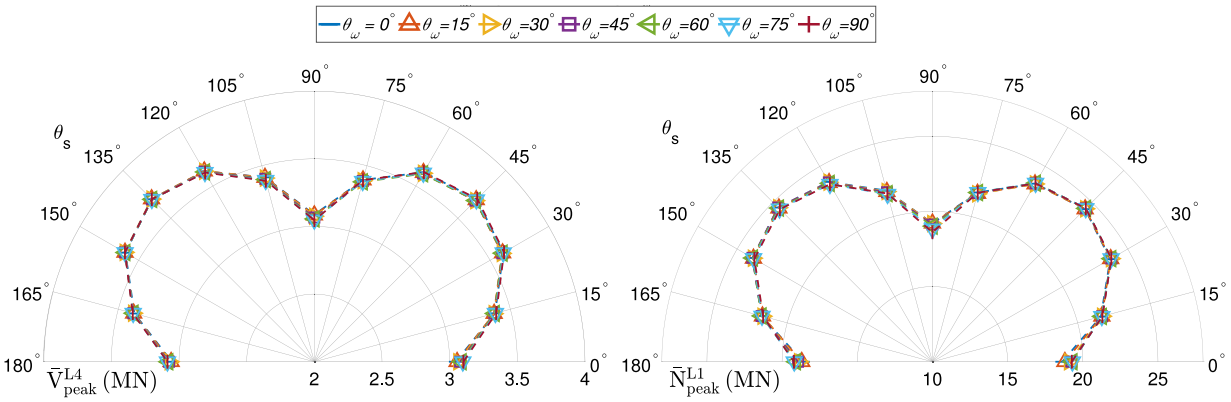

Fig. 17. Average peak response values in terms of shear and axial forces at leg levels 4 and 1, respectively, for the different wind and shaking directions in parked mode.

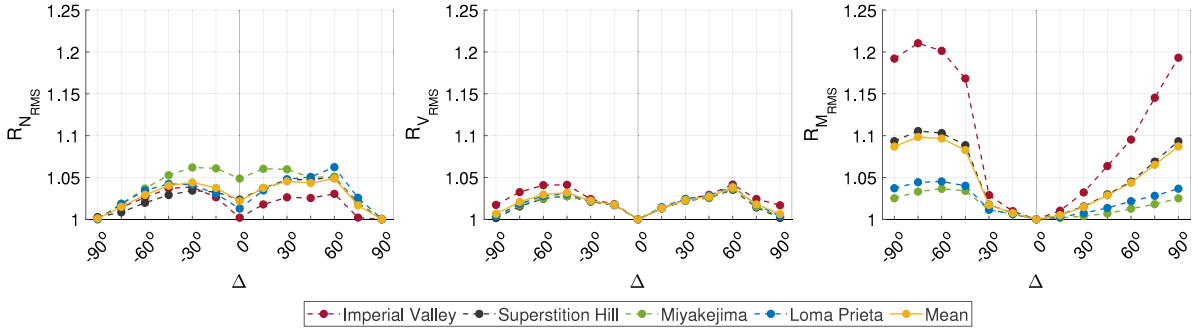

Fig. 18. Amplification ratios for axial forces, shear forces and bending moments at leg levels 1, 4 and pile head, respectively, for the different misalignment angles between wind and ground motion directions in parked mode.

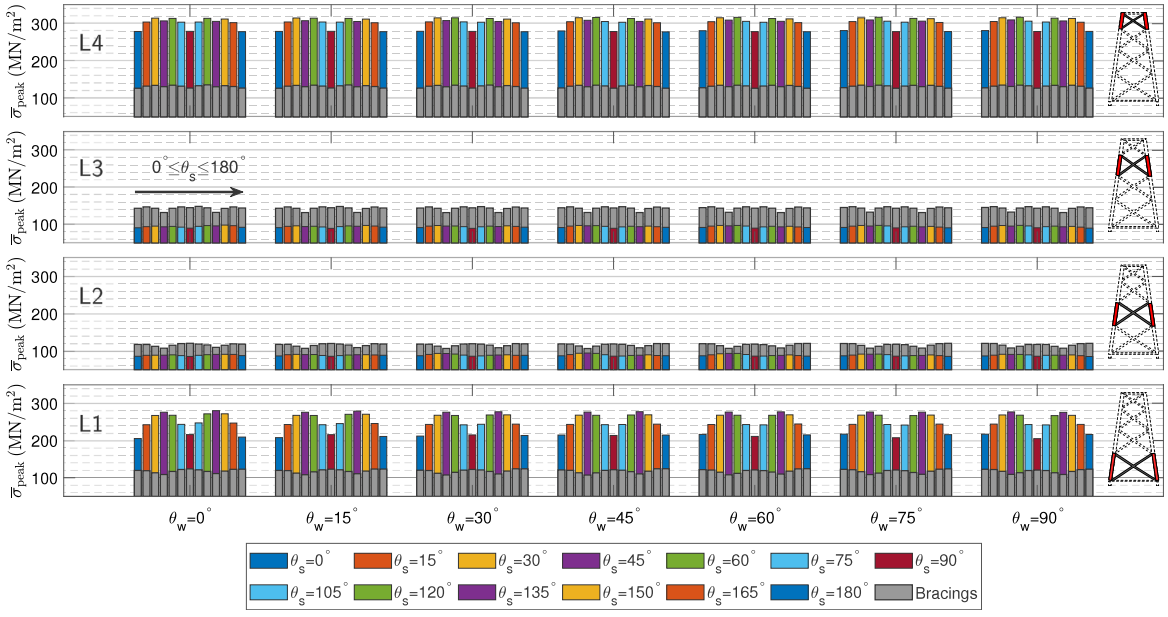

Fig. 19. Average peak response in terms of von Mises stress in the substructure for the different wind and shaking directions in parked mode. Colour bars are used for stresses in leg members, and grey bars for stresses in the bracing elements (θ_s according to the position).

shaking directions is 0°. The worst-case scenarios in terms of axial and shear amplification ratios are found for $30° \leq |\Delta| \leq 60°$. It is important to note that the highest bending moments ratios are obtained in parked mode. The highest bending moments ratios are found when the range is $60° \leq |\Delta| \leq 90°$.

Fig. 19 shows the average peak von Mises stresses in the different levels of the jacket (considering legs and bracings). In contrast to power production, the maximum values in each wind direction are quite similar. Unlike in the emergency shutdown and the power production modes, the increase in peak response when the earthquake acts along

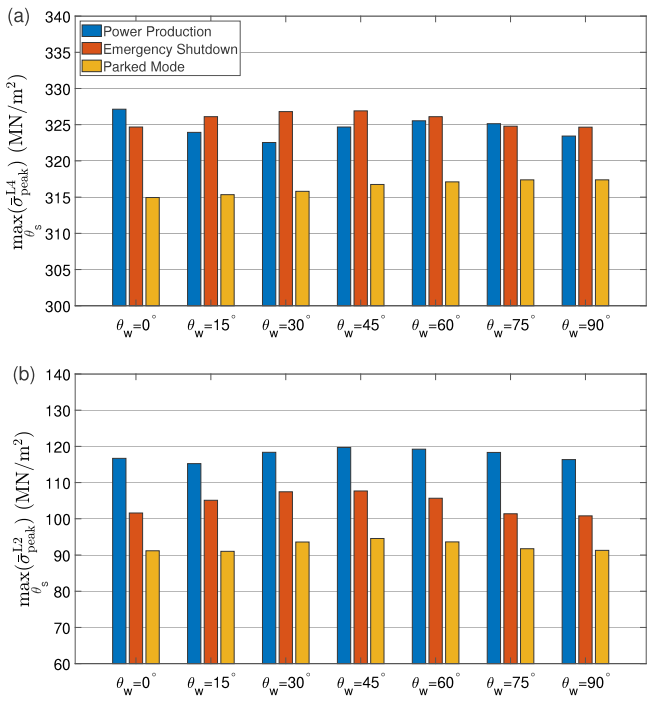

Fig. 20. Maximum average peak von Mises stresses at levels 4 (a) and 2 (b) of the legs for different operational modes among all the wind and shaking directions in the study.

the side-to-side direction is not observed. For instance, when $\theta_w = 0°$, similar stresses are observed when the shaking direction (θ_s) is 0°, 90° or 180°. The von Mises stresses are lower than those obtained during power production. The parked mode is beneficial in terms of stresses at the bracing and leg elements of the jacket.

4.2.4. Comparison between operational modes

A comparison among the maximum average peak von Mises stresses obtained at levels 4 ($\bar{\sigma}^{L4}_{\text{peak}}$) and 2 ($\bar{\sigma}^{L2}_{\text{peak}}$) of the legs for the different operational scenarios is shown in Fig. 20 for all the wind directions considered in the study. More precisely, the maximum value of those obtained among all ground shaking directions ($\max\{\bar{\sigma}_{\text{peak}}(\theta_s) : \theta_s = 0, 15 .. 90°\}$) is presented in the figure for levels 2 and 4 and for each operational mode and wind direction.

The power production and the emergency stop modes are the operational modes that produce the highest average stress at the upper part of the legs. The reason why the emergency stop situation is sometimes the worst-case scenario can be understood by the fact that, although emergency stop is executed from the instant the first peak of the earthquake is noticed (with the largest shocks arriving later) and the influence of the wind load is vanishes gradually, the disconnection of the rotor causes a transitory increase in the peak internal forces within the jacket substructure. On the other hand, the greatest stress relative variations between the different operational modes arise along the central part of the legs, where the stress are the lowest. In this case, the power production mode is the one that produces always the highest average peak stresses. The lowest stresses along the whole length of the legs, are obtained, as expected, for the parked mode, situation at which the effect of the aerodynamic loads is minimal. In fact, the assumption of the parked mode for the structural design would lead to an underestimation of 6% at the top and 28% at the central levels of the legs, in terms of von Mises stress.

Figs. 21 shows the average von Mises stresses of the leg and bracing elements separately, at the points where the maximum stresses are obtained for the different levels of the substructure (points *a* to *e*, whose locations are depicted in the figure using red dots). The results presented in the figure correspond to $\theta_w = 0°$, and to different shaking directions ($\theta_s = 0°, 45°, 90°$). The three different modes of operation in this study are represented with three different colours and symbols. In parallel, Table 5 presents the percentage variations between the average peak von Mises stresses obtained during emergency stop compared to those obtained in power production ($\delta_{\text{ES-PP}}$), and obtained in parked mode compared to those obtained in power production ($\delta_{\text{PM-PP}}$), at the five key points *a* to *e* along the legs mentioned above.

Table 5
Variations of average peak von Mises stress at legs for the different operational modes.

Point	$\theta_s = 0°$		$\theta_s = 45°$		$\theta_s = 90°$	
	$\delta_{\text{ES-PP}}$	$\delta_{\text{PM-PP}}$	$\delta_{\text{ES-PP}}$	$\delta_{\text{PM-PP}}$	$\delta_{\text{ES-PP}}$	$\delta_{\text{PM-PP}}$
a	−0.2%	1.2%	−2.4%	1.3%	6.6%	10.5%
b	9.9%	23.8%	5.0%	21.2%	11.6%	24.6%
c	9.6%	22.7%	9.8%	24.9%	20.1%	37.7%
d	10.3%	9.0%	26.9%	9.5%	3.8%	9.7%
e	6.1%	3.1%	2.2%	1.3%	7.9%	9.6%

As already mentioned, the most stressed parts of the support structure are the sections of the legs connected to the transition piece and to the pile, as evidenced by the significantly higher stress levels at the top and bottom compared to the central levels of the jacket. The smallest average stresses in the legs are obtained when the shaking acts along the fore–aft direction ($\theta_s = 0°$, left plots of the figure), while the largest stresses are obtained when the earthquake acts along the diagonal direction of the jacket ($\theta_s = 45°$). At the points of highest stresses (top and bottom of the legs) the variations in stresses for the different modes tend to be small (< 10% in most cases), but in the intermediate parts of the legs, where the stresses are lower, the average peak von Mises stresses can vary up to 38% when comparing power production with parked mode, and up to 27% when comparing power production with emergency shutdown. A quite similar trend is observed in the bracing levels between each of them, but with the highest von Mises stresses arising at the level 3 in this case. As expected, the parked mode provides the lowest stresses in all cases. An interesting fact is that the highest average peak stresses are not always obtained for the same operational mode, as discussed above, depending of the wind and shaking directionality.

Finally, in order to make a comparison between the internal forces obtained at the pile head for different operational modes, Fig. 22 presents the average peak of bending moments and axial forces at the pile head as function as the misalignment between wind and shaking direction (Δ). The bending moments of the jacket substructure, for all cases considered in this work, reach their maximum value at the pile head.

The results show that in terms of bending moments, the worst-case scenario corresponds to the parked mode, specifically to the case when the shaking acts along the side-to-side direction, i.e., $\Delta = 90°$, although the difference with respect to the power production mode is only of 1.5%. Focusing on the misalignment between wind and shaking directions, the highest values are obtained for $75° \leq \Delta \leq 90°$. Nevertheless, these ranges do not correspond to those observed for maximum axial forces. The highest axial forces at the pile head are found for $0° \leq \Delta \leq 30°$ during power production. In particular, the peak axial force is obtained for $\Delta = 0°$. The difference with respect to the parked mode in this case is 6.3%. The results show that the average peak internal forces change by up to 4% in magnitude depending on the alignment between environmental and seismic loads, while the variability between operational modes reaches 8%.

5. Conclusions

This study outlined the main conclusions drawn from an analysis of the influence of the different operational modes (power production,

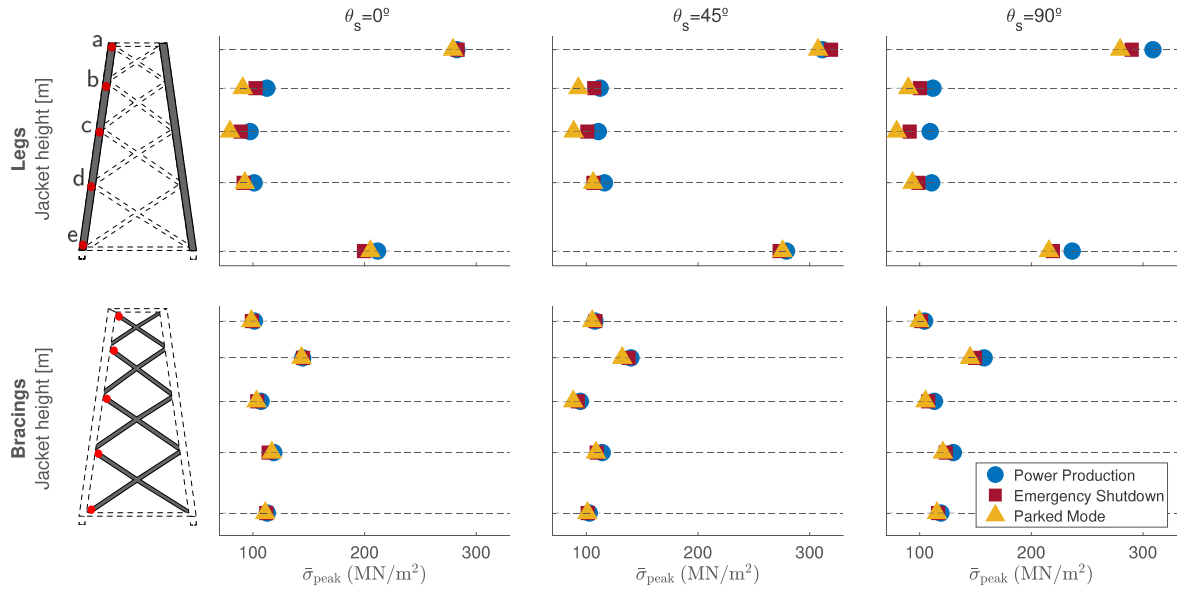

Fig. 21. Average peak von Mises stress at legs and bracings at the different levels of the substructure, for the different operational modes, for $\theta_w = 0°$ and for different shaking directions ($\theta_s = 0°, 45°, 90°$).

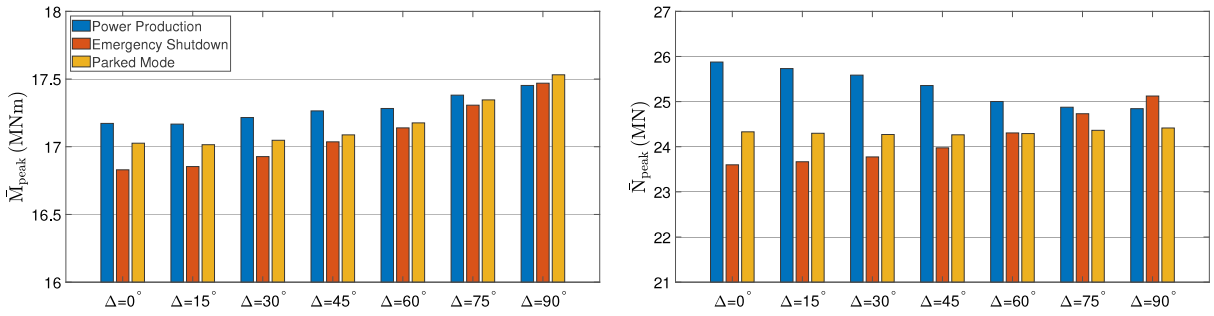

Fig. 22. Average peak bending moments and axial forces at the pile head for different operational modes considering the misalignment (Δ) between wind and shaking directions in this study.

emergency shutdown and parked mode) and of the effect of the wind and seismic shaking directionality on the seismic structural response of the NREL 5 MW offshore wind turbine founded on the OC4-project jacket support structure. The set of cases included thirteen different seismic ground motion directions, seven wind directions, and four different earthquake records, resulting in a total of 1113 time-domain simulations performed using a modified OpenFAST model that includes soil–structure interaction, kinematic interaction and multi-support input motion. Based on the results, the following conclusions can be drawn:

- Emergency shutdown is not necessarily beneficial in terms of reducing peak accelerations at the nacelle. The maximum accelerations in this case are 30% higher than during power production. On the other hand, the smallest peak accelerations are obtained for the power production mode when the earthquake acts along the fore–aft direction. This is due to the higher aerodynamic damping, which has a beneficial effect by reducing the magnitude of the vibrations induced by the earthquake. Emergency shutdown is also the mode that tends to produce the largest oscillations in displacements at the tower top.
- Due to the geometry of the four-legged jacket-supported OWT, the maximum internal forces and von Mises stresses are usually found when the ground shaking acts along one of the diagonals of the jacket structure and not aligned with the wind direction in the three operational modes. The shaking direction tends to have a larger influence on the peak internal forces than wind directionality. A greater influence of the misalignment between wind and shaking directions on the stresses at the jacket is observed in power production mode than in emergency shutdown and parked modes.
- The relative differences in the structural response in terms of maximum internal forces and stresses in the jacket structural members, when the turbine is working in the different operational modes, tend to be smaller than the differences in terms of accelerations at tower top.
- At the points of highest stresses (top and bottom of the legs) the percentage variations of the average peak von Mises stress for the different modes tend to be relatively small (<10% in most cases). On the contrary, along the intermediate parts of the legs, where the stresses are the lowest, the average peak von Mises stresses can vary up to 38% when comparing power production with

parked mode, and up to 27% when comparing power production with emergency shutdown.

- The maximum stresses appear almost always in the case of power production, with the exception of the top part of the legs, where higher stresses arise during emergency shutdown in several cases.
- The highest bending moments at the pile head are obtained when the shaking acts in side-to-side direction for the three modes. In this case, the maximum is obtained in parked mode. However, the maximum axial forces are observed when the misaligment between wind and shaking directions is 0° during power production. For emergency shutdown and parked modes, the maximum axial forces arise when the misaligment is 90°. In any case, the differences between the peak internal forces obtained for the different modes of operation, at the pile head, are below 8%.

In short, the results show that the structural response of the jacket is, under the occurrence of an earthquake, significantly influenced by the operational mode of the turbine at the time of arrival of the seismic waves, and by the misalignment between environmental and seismic loads. The magnitude of these influences has been quantified for the particular cases studied in this paper.

CRediT authorship contribution statement

Carlos Romero-Sánchez: Writing – review & editing, Writing – original draft, Visualization, Validation, Supervision, Software, Methodology, Investigation, Funding acquisition, Formal analysis, Conceptualization. **Luis A. Padrón:** Writing – review & editing, Validation, Supervision, Software, Methodology, Funding acquisition, Formal analysis, Conceptualization.

Declaration of competing interest

The authors declare that they have no known competing financial interests or personal relationships that could have appeared to influence the work reported in this paper.

Acknowledgements

This research was funded by the Ministerio de Ciencia, Innovación y Universidades, Spain and the Agencia Estatal de Investigación of Spain (MCIN/AEI/ 10.13039/501100011033) and FEDER, Spain through research project PID2020-120102RB-I00. In addition, C. Romero-Sánchez is a recipient of the research fellowship (TESIS2022010011), from the Program of predoctoral fellowships from the Consejería de Economía, Conocimiento y Empleo (Agencia Canaria de la Investigación, Innovación y Sociedad de la Información) of the Gobierno de Canarias and Fondo Social Europeo. The authors are grateful for this support.

References

Álamo, G., Bordón, J., Aznárez, J., 2021. On the application of the beam model for linear dynamic analysis of pile and suction caisson foundations for offshore wind turbines. Comput. Geotech. 134, 104107.

Álamo, G., Martínez-Castro, A., Padrón, L., Aznárez, J., Gallego, R., Maeso, O., 2016. Efficient numerical model for the computation of impedance functions of inclined pile groups in layered soils. Eng. Struct. 126, 379–390.

Alati, N., Failla, G., Arena, F., 2015. Seismic analysis of offshore wind turbines on bottom-fixed support structures. Phil. Trans. R. Soc. A 373 (2035), 20140086.

Arias, A., Hansen, R., 1970. Seismic design for nuclear power plants. In: A Measure of Earthquake Intensity. MIT Press Cambridge, pp. 438–483.

Asareh, M., Schonberg, W., Volz, J., 2016. Effects of seismic and aerodynamic load interaction on structural dynamic response of multi-megawatt utility scale horizontal axis wind turbines. Renew. Energy 86, 49–58.

Carbonari, S., Morici, M., Dezi, F., Leoni, G., 2018. A lumped parameter model for time-domain inertial soil-structure interaction analysis of structures on pile foundations. Earthq. Eng. Struct. Dyn. 47 (11), 2147–2171.

Cheng, Y., Luo, Y., Wang, J., Dai, K., Wang, W., El Damatty, A., 2023. Fragility and vulnerability development of offshore wind turbines under aero-hydro loadings. Eng. Struct. 293, 116625.

Chopra, A., 2017. Dynamics of Structures. Theory and Applications to Earthquake Engineering, Seventh ed. Pearson.

Clough, R., Penzien, J., 1995. Dynamics of Structures, third ed. Computers & Structures.

Damiani, R., Jonkman, J., Hayman, G., 2015. SubDyn User's Guide and Theory Manual. Technical Report, National Renewable Energy Lab.(NREL), Golden, CO (United States).

DNV, 2014. Design of Offshore Wind Turbine Structures. Offshore Standard DNV-OS-J101. DetNorske Veritas AS.

DNV, 2016. Loads and Site Conditions for Wind Turbines. Offshore Standard DNV-ST-0437. DetNorske Veritas AS.

Dobry, R., Idriss, I., Ng, E., 1978. Duration characteristics of horizontal components of strong-motion earthquake records. Bull. Seismol. Soc. Am. 68 (5), 1487–1520.

Eurcode 8 - Part 5, 2018. Eurocode 8: Design of Structures for Earthquake Resistance – Part 5: Foundations, Retaining Structures and Geotechnical Aspects. European Committee for Standardization.

Eurocode 3 - Part 1-6, 2007. Eurocode 3: Design of Steel Structures – Part 1-6: Strength and Stability of Shell Structures. European Committee for Standardization.

Global Wind Energy Council, 2023. Global Offshore Wind Report 2023. Technical Report, GWEC, Brussels, Belgium.

IEC, 2020. 61400-1:2020 Wind Energy Generation Systems - Part 1: Design Requirements. International Electrotechnical Commission.

IEC, 2021. 61400-3-1:2021 Wind Energy Generation Systems - Part 3-1: Design Requirements for Fixed Offshore Wind Turbines. International Electrotechnical Commission.

Ishihara, T., Iida, Y., Wang, L., 2024. Numerical study of combined seismic and aerodynamic loads on wind turbine support structures using coupled and uncoupled approaches. Structures 60, 105886.

ISO 19901-2, 2022. International Organization for Standardization. ISO 19901-2:2022 Petroleum and Natural Gas Industries — Specific Requirements for Offshore Structures — Part 2: Seismic Design Procedures and Criteria. International Organization for Standardization.

James, M., Haldar, S., 2022. Seismic vulnerability of jacket supported large offshore wind turbine considering multidirectional ground motions. Structures 43, 407–423.

Jonkman, B., 2009. TurbSim User's Guide: Version 1.50. Technical Report, National Renewable Energy Lab.(NREL), Golden, CO (United States).

Jonkman, J., Butterfield, S., Musial, W., Scott, G., 2009. Definition of a 5-MW Reference Wind Turbine for Offshore System Development. Technical Report, National Renewable Energy Lab.(NREL), Golden, CO (United States).

Jonkman, J., Musial, W., 2010. Offshore Code Comparison Collaboration (OC3) for IEA Wind Task 23 Offshore Wind Technology and Deployment. National Renewable Energy Lab.(NREL), Golden, CO (United States).

Ju, S.-H., Huang, Y.-C., 2019. Analyses of offshore wind turbine structures with soil-structure interaction under earthquakes. Ocean Eng. 187, 106190.

Katsanos, E., Sanz, A., Georgakis, C., Thöns, S., 2017. Multi-hazard response analysis of a 5MW offshore wind turbine. Procedia Eng. 199, 3206–3211.

Løken, I., Kaynia, A., 2019. Effect of foundation type and modelling on dynamic response and fatigue of offshore wind turbines. Wind Energy 22 (12), 1667–1683. http://dx.doi.org/10.1002/we.2394.

Meng, J., Dai, K., Zhao, Z., Mao, Z., Camara, A., Zhang, S., Mei, Z., 2020. Study on the aerodynamic damping for the seismic analysis of wind turbines in operation. Renew. Energy 159, 1224–1242.

Mo, R., Cao, R., Liu, M., Li, M., Huang, Y., 2021. Seismic fragility analysis of monopile offshore wind turbines considering ground motion directionality. Ocean Eng. 235, 109414.

Moriarty, P., Hansen, A., 2005. AeroDyn Theory Manual. Technical Report, National Renewable Energy Lab., Golden, CO (US).

Musial, W., Spitsen, P., Beiter, P., Duffy, P., D.M., H., Hammond, R., Shields, M., Marquis, M., 2023. Offshore Wind Market Report: 2023 Edition. Technical Report, National Renewable Energy Laboratory(NREL), Golden, CO (United States).

National Renewable Energy Laboratory, 2024. OpenFAST Documentation. Release v3.5.2. National Renewable Energy Laboratory, https://openfast.readthedocs.io/en/main/. Code published at https://github.com/OpenFAST/openfast.

National Research Institute for Earth Science and Disaster Resilience (K-NET), 2022. Strong-motion seismograph networks. Available online: https://www.kyoshin.bosai.go.jp/. (Accessed on 20 November 2022).

Pacific Earthquake Engineering Research Center (PEER), 2022. NGA-West2 ground motion database. Available online: ngawest2.berkeley.edu/. (Accessed 20 November 2022).

Padrón, L., Carbonari, S., Dezi, F., Morici, M., Bordón, J., Leoni, G., 2022. Seismic response of large offshore wind turbines on monopile foundations including dynamic soil–structure interaction. Ocean Eng. 257, 111653.

Romero-Sánchez, C., Padrón, L., 2022. Implementation of ground input motion and dynamic soil-structure interaction into openfast for the seismic analysis of offshore wind turbines. In: Congress on Numerical Methods in Engineering. CMN 2022, International Center for Numerical Methods in Engineering (CIMNE).

Romero-Sánchez, C., Padrón, L., 2023. An implementation of multi-support input motion into openfast for the earthquake analysis of offshore wind turbines. COMPDYN Proc..

Romero-Sánchez, C., Padrón, L., 2024. Influence of wind and seismic ground motion directionality on the dynamic response of four-legged jacket-supported Offshore Wind Turbines. Eng. Struct. 300, 117191.

Vorpahl, F., Popko, W., Kaufer, D., 2011. Description of a Basic Model of the "UpWind Reference Jacket" for Code Comparison in the OC4 Project under IEA Wind Annex XXX, vol. 450, Fraunhofer Institute for Wind Energy and Energy System Technology (IWES), Germany.

Xi, Y., Lin, K., Pan, J., Sun, L., Li, H., Wang, Z., 2023. Bending moment characteristic analysis of utility-scale onshore wind turbine blades based on monitoring data. Eng. Struct. 294, 116714.

Yang, Y., Bashir, M., Li, C., Wang, J., 2019. Analysis of seismic behaviour of an offshore wind turbine with a flexible foundation. Ocean Eng. 178, 215–228.

Zuo, H., Bi, K., Hao, H., 2018. Dynamic analyses of operating offshore wind turbines including soil-structure interaction. Eng. Struct. 157, 42–62.

Zuo, H., Bi, K., Hao, H., Li, C., 2019. Influence of earthquake ground motion modelling on the dynamic responses of offshore wind turbines. Soil Dyn. Earthq. Eng. 121, 151–167.